Magnetic Actuation of Flexible Microelectrode Arrays for Neural Activity Recordings

Lei Gao,[†,‡,∇] Jinfen Wang,[†,∥,∇] Shouliang Guan,[†,‡] Mingde Du,[†,‡,#] Kun Wu,[⊥] Ke Xu,[†,‡] Liang Zou,[†,‡] Huihui Tian,[†] and Ying Fang*[,†,‡,§]

[†]CAS Key Laboratory of Biomedical Effects of Nanomaterials and Nanosafety, CAS Center for Excellence in Nanoscience, National Center for Nanoscience and Technology, Beijing 100190, P. R. China

[‡]University of Chinese Academy of Sciences, Beijing 100049, P. R. China

[§]CAS Center for Excellence in Brain Science and Intelligence Technology, Chinese Academy of Sciences, Shanghai 200031, P. R. China

[∥]State Key Laboratories of Transducer Technology, Chinese Academy of Sciences, Beijing 100190, P. R. China

[⊥]State Key Laboratory of High Temperature Gas Dynamics, Institute of Mechanics, Chinese Academy of Sciences, Beijing 100190, P. R. China

[#]Department of Electronics and Nanoengineering, Aalto University, Espoo FI-00076, Finland

S Supporting Information

ABSTRACT: Implantable microelectrodes that can be remotely actuated via external fields are promising tools to interface with biological systems at a high degree of precision. Here, we report the development of flexible magnetic microelectrodes (FMμEs) that can be remotely actuated by magnetic fields. The FMμEs consist of flexible microelectrodes integrated with dielectrically encapsulated FeNi (iron−nickel) alloy microactuators. Both magnetic torque- and force-driven actuation of the FMμEs have been demonstrated. Nanoplatinum-coated FMμEs have been applied for *in vivo* recordings of neural activities from peripheral nerves and cerebral cortex of mice. Moreover, owing to their ultrasmall sizes and mechanical compliance with neural tissues, chronically implanted FMμEs elicited greatly reduced neuronal cell loss in mouse brain compared to conventional stiff probes. The FMμEs open up a variety of new opportunities for electrically interfacing with biological systems in a controlled and minimally invasive manner.

KEYWORDS: *flexible microelectrode, magnetic actuation, nanoscale roughness, neural recording, inflammatory response*
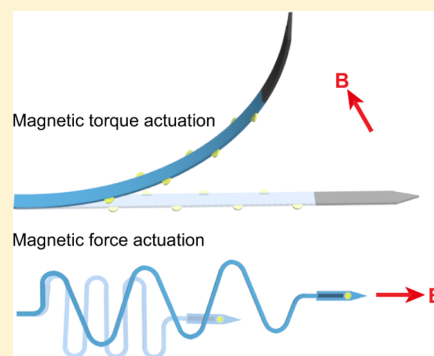
Implantable microelectrodes that transduce ionic signals to electronic signals are among the most widely applied tools for *in vivo* recordings of neural activities from peripheral and central nervous systems.[1−3] Furthermore, implantable microelectrodes have been used clinically for the treatment of neurological disorders, such as Parkinson's disease.[4] The importance of implantable microelectrodes has also been recognized in the development of peripheral nerve interfaces for prosthetic control.[5] Conventional implantable microelectrodes are based on metals or silicon with elastic moduli in the range of 10^2 GPa, whereas the elastic moduli of peripheral and central nervous systems are in the MPa to kPa range.[6,7] The large mechanical mismatch between the implanted rigid microelectrodes and neural tissues results in tissue−electrode micromotion and chronic inflammatory responses.[8−11] Recently, flexible microelectrodes based on thin polymer substrates have been studied extensively due to their improved mechanical compliance to biological tissues.[12−15] Compared to rigid microelectrodes, flexible microelectrodes have demonstrated greatly reduced immune responses in chronic studies.[14,15] However, the accurate *in*

vivo positioning of flexible microelectrodes presents an extremely challenging situation because of their susceptibility to buckling instability under in-plane compression. A variety of strategies, including syringe injection,[14] removable insertion shuttles,[12,15] polymer molds,[16,17] and integrated microfluidic devices,[18] have been used to temporarily increase the rigidity of flexible microelectrodes for *in vivo* positioning.

Remotely actuated microscale structures, such as micro- and nanoparticles, can interact with biological systems down to cellular scales and are of great importance for a wide variety of *in vitro* and *in vivo* applications, including the precise manipulation of single cells and the targeted delivery of drugs.[19−21] Several actuation methods have been developed, including optical,[22] electric,[23] thermal,[24] magnetic,[21,25] and chemical fuel-driven actuation.[26] Among these methods, magnetic actuation has been considered as one of the most
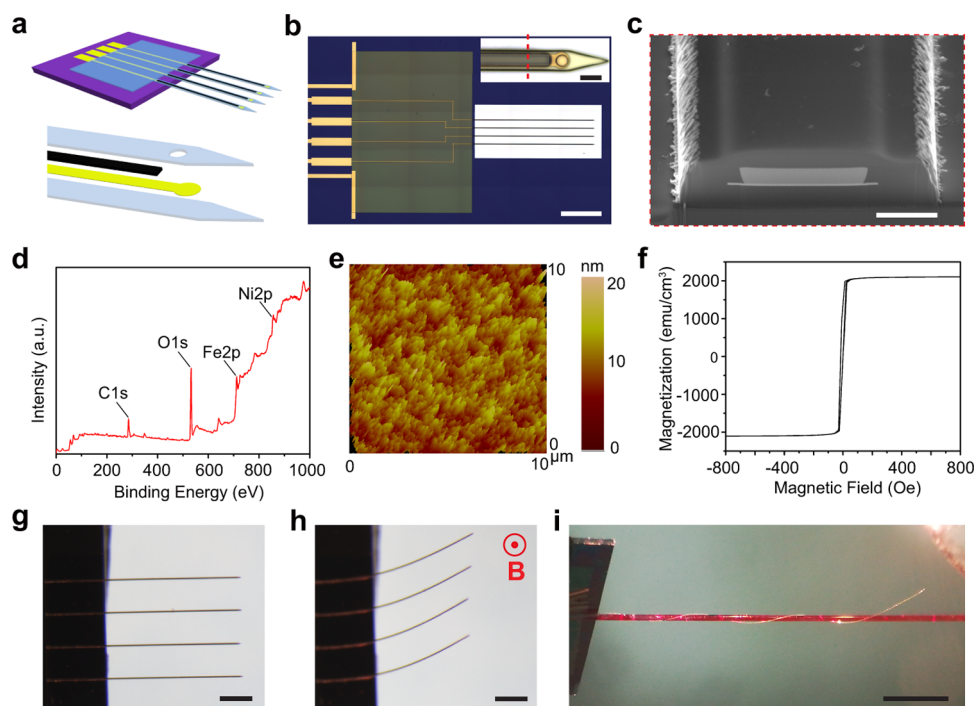
Figure 1. Magnetic torque-driven actuation of FMμEs. (a) Schematic of the layout of FMμEs. The Si/SiO$_2$ substrate, PI layers, Au conductive layer, and FeNi alloy layer are shown in purple, gray, yellow, and black color, respectively. (b) As-fabricated FMμEs. Scale bar, 1 mm. Inset, microphotoimage of an FMμE with a 10-μm-diameter recording site. Inset scale bar, 20 μm. (c) Cross-sectional SEM image of an FMμE, indicated by the red dashed line in (b). Scale bar, 5 μm. (d) XPS of FeNi alloy layer. (e) AFM image of FeNi alloy layer. (f) Magnetization versus magnetic field (M–H) loop at room temperature. (g) Released FMμEs in air. Scale bar, 500 μm. (h) Magnetic torque-driven actuation of FMμEs by a rotating permanent magnet. The direction of magnetic field is perpendicular to the paper surface. Scale bar, 500 μm. (i) A 15-mm-long FMμE was helically wound around a 200-μm-diameter optical fiber by a rotating permanent magnet. The optical fiber was dyed in red color. Scale bar, 2 mm.

promising means for *in vivo* applications because, unlike electric fields and light, magnetic fields are not attenuated or distorted by biological fluids and tissues.[27] Therefore, magnetic fields can penetrate deep into the body without causing adverse health effects. In addition, compared to chemical fuel-driven actuation, magnetic actuation does not use or produce harmful chemicals *in vivo*. Over the past two decades, a variety of microscale magnetic particles have been prepared and applied for targeted *in vivo* imaging and therapy.[28,29] For example, magnetite magnetic nanoparticles can be remotely guided by external magnets to targeted areas for specific drug delivery, such as brain-targeted delivery of the anti-Alzheimer's drug tacrine.[30] Helical magnetic micro- and nanoswimmers can be propelled in low Reynolds number fluids by rotating magnetic fields.[31,32] Moreover, real-time, closed-loop navigation of magnetic microparticles has also been demonstrated using the propulsion gradient coils in a magnetic resonance imaging (MRI) scanner.[33]

The integration of sensing and actuating functions in microscale devices can give rise to innovative biological applications, including new biosensing platforms with the capability of remote manipulation amid complex biological environments. Here, we report FMμEs that feature the integration of neural recording microelectrodes and magnetic microactuators. The FMμEs can be remotely actuated by magnetic forces for *in vivo* interfacing with biological systems. Neural activity recordings from both mouse peripheral nerves and cerebral cortex have been demonstrated with the FMμEs. Immunohistological studies have further confirmed that chronically implanted FMμEs can form stable interfaces with the nervous systems.

Figure 1a shows the schematic of FMμEs consisting of recording microelectrodes and magnetic microactuators. The FMμEs were fabricated on the Si/SiO$_2$ substrates with patterned sacrificial aluminum (Al) layers (Figure S1). As shown in Figure 1b, the microelectrodes are sandwiched between 2-μm-thick polyimide (PI) layers (except the recording sites and bonding pads). To achieve remote magnetic actuation, FeNi alloy microactuators were selectively formed at the end-points of the microelectrodes by electro-deposition and subsequently encapsulated with PI layers to protect them from *in vivo* degradation. FeNi alloy was chosen because of its high saturation magnetization and low coercivity.[34,35] Figure 1c shows a focused ion beam (FIB)-prepared cross-sectional scanning electron microscopy (SEM) image of a 2-μm-thick and 10-μm-wide FeNi alloy layer that has been completely encapsulated by PI.

Next, we characterized the structural and magnetic properties of the electrodeposited FeNi alloy layers. The surface chemical composition of the FeNi alloy was studied by X-ray photoelectron spectroscopy (XPS) (Figures 1d and S2a,b). The peaks of Fe 2p$_{3/2}$ and Fe 2p$_{1/2}$ are located at 711.4 and 724.6 eV (Figure S2a), respectively.[36] The peaks at 856.0 and 873.7 eV are attributed to Ni 2p$_{3/2}$ and Ni 2p$_{1/2}$ (Figure S2b), respectively. The surface Fe/Ni atomic ratio was calculated to be 47.7/52.3 from the XPS spectra. Figure S2c shows the X-ray diffraction (XRD) pattern recorded from the FeNi alloy. The peaks located at 43.88° and 50.77° were assigned to diffraction from the (111) and (200) planes, respectively, of a face-centered cubic (fcc) lattice with a unit cell size of 0.357 nm.[35] The surface morphology of the FeNi alloy was characterized with atomic force microscopy (AFM) (Figure 1e), which
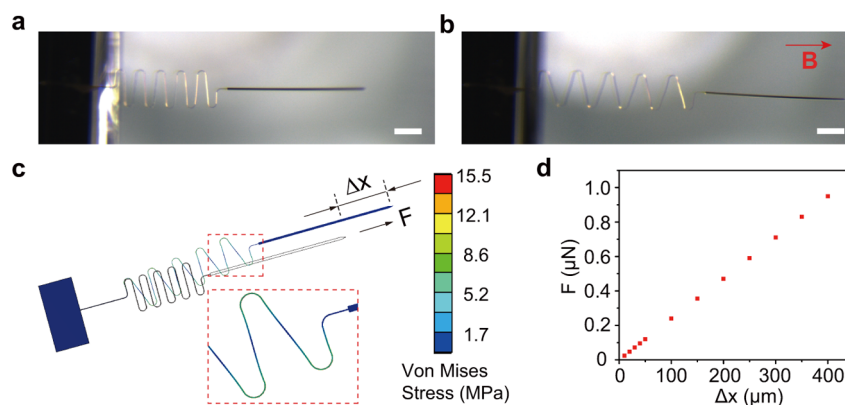
Figure 2. Magnetic force-driven actuation of FMμE. (a) Microphotoimage of an FMμE consisting of a magnetic head and a stretchable serpentine microspring. Scale bar, 200 μm. (b) Microphotoimage showing that the magnetic force stretched the microspring by up to 400 μm. The permanent magnet was placed at a distance of ca. 2 mm, and the red arrow indicates the direction of magnetic field. Scale bar, 200 μm. (c) Mechanical simulation of the stress distribution on a stretched FMμE. (d) Numerical value of the force (F) as a function of the displacement (Δx).
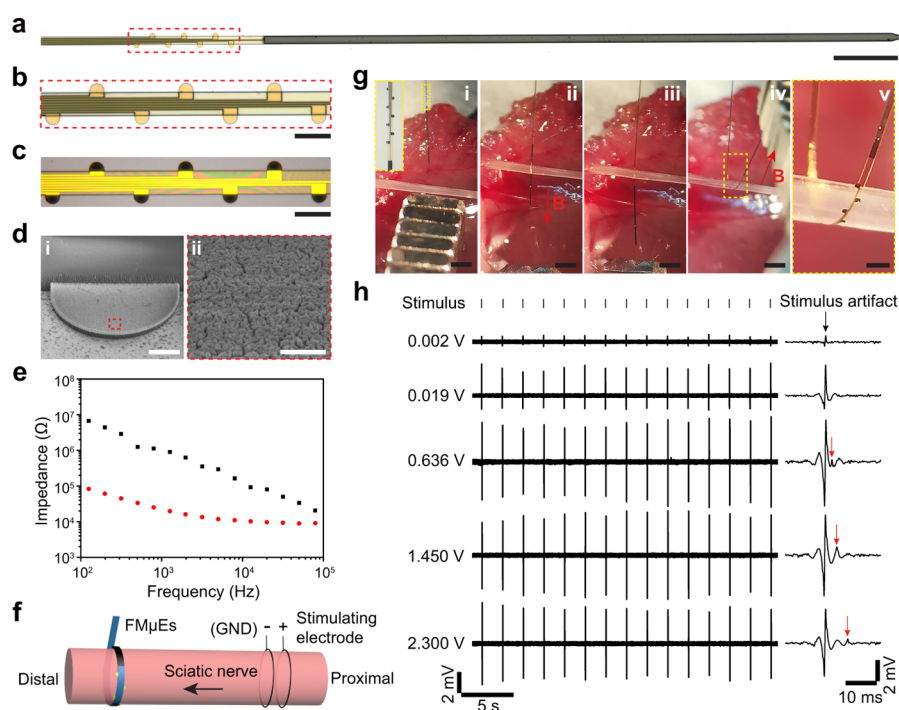

Figure 3. *In vivo* neural activity recording from the sciatic nerve. (a) FMμE array for neural activity recordings from mouse sciatic nerve. Scale bar, 500 μm. (b) Zoom-in view of the recording sites as marked by the red dashed box in (a). Scale bar, 100 μm. (c) Recording sites after nanoplatinum deposition. Scale bar, 100 μm. (d) (i) SEM image of a recording site coated with nanoplatinum. Scale bar, 10 μm. (ii) Zoom-in view of the nanoplatinum as marked by the red dashed box in (i). Scale bar, 1 μm. (e) Electrochemical impedance spectroscopy (EIS) of the FMμE array before (black squares) and after (red dots) modification with nanoplatinum, respectively. (f) Schematic of the setup for sciatic nerve recordings. (g) Remote magnetic actuation of the FMμE array to interface with the sciatic nerve, and the red arrow indicates the direction of magnetic field. Scale bars, 1 mm in (i−iv) and 200 μm in (v). (h) Electrical recordings of stimulated CAPs (indicated by the red arrows). The signals were band-pass filtered at 250−2000 Hz. The frequency and duration of the stimulus voltage were 0.5 Hz and 0.2 ms, respectively.

revealed a relatively small root-mean-square (RMS) roughness of ~20 nm. The magnetic properties of the FeNi alloy microactuators in the FMμEs were studied by measuring the magnetization versus magnetic field (M−H) loop at room temperature. As shown in the hysteresis loop in Figure 1f, the electrodeposited FeNi alloy microactuators exhibited high saturation magnetization of 2070 emu/cm^3 and low coercivity of below 20 Oe.[37]

The good soft magnetic properties of FMμEs make them suitable for magnetic actuation applications. The magnetic torque, $\overrightarrow{\tau_m}$, and magnetic force, $\overrightarrow{F_m}$, exerted on a magnetized structure can be expressed as follows:[21,27]

$$\overrightarrow{\tau_m} = V_m \vec{M} \times \vec{B}$$

and

$$\overrightarrow{F_m} = V_m(\vec{M}\cdot\nabla)\vec{B}$$

where $\vec{M}$ is the magnetization, V_m is the volume, and $\vec{B}$ is the magnetic flux density. From the relationship, we can see that the magnetic torque is proportional to the magnetic field and
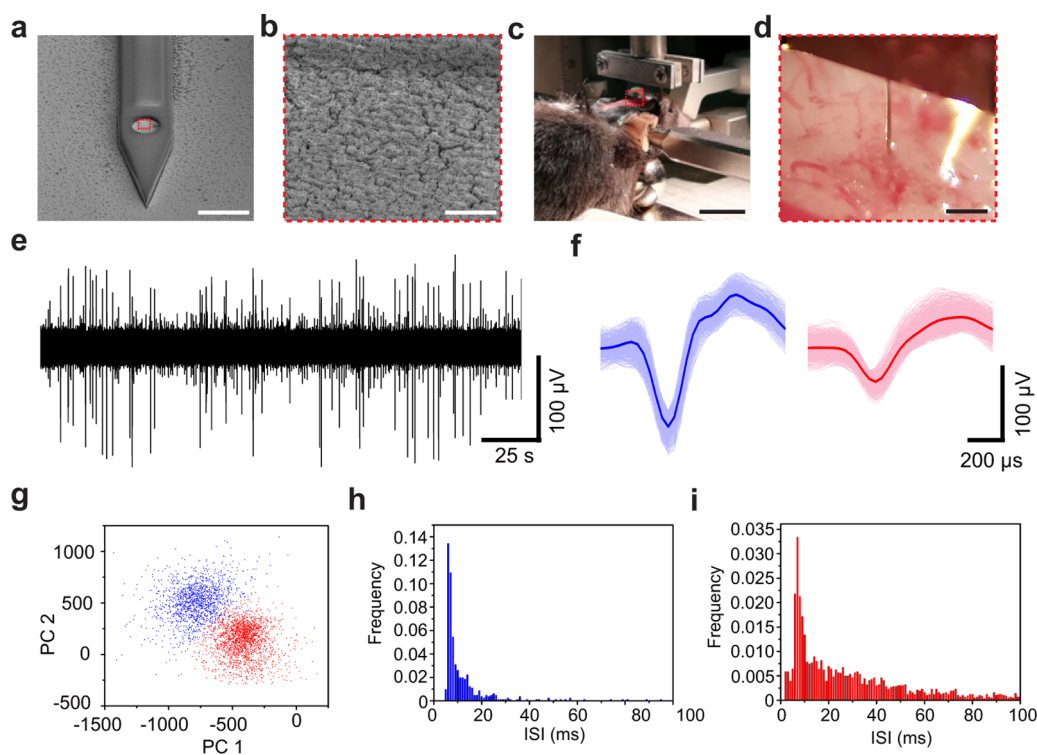
Figure 4. *In vivo* neural activity recordings from cerebral cortex. (a) SEM of an FMμE. Scale bar, 20 μm. (b) Micromorphology of the nanoplatinum coating as marked by the red dashed box in (a). Scale bar, 1 μm. (c) Implanted FMμE in mouse cerebral cortex. Scale bar, 10 mm. (d) Zoom-in view of the implanted FMμE as marked by the red dashed box in (c). Scale bar, 200 μm. (e) Representative AP trace recorded by an FMμE from M2 cortex. (f) Aligned and mean spike waveforms of sortable spike 1 (blue) and spike 2 (red). (g) Principal component analysis (PCA) showing two distinct clusters. (h) Interspike-interval (ISI) histogram of spike 1. (i) ISI histogram of spike 2.

that the magnetic force is proportional to the gradient of the magnetic field. We first investigated the magnetic torque-driven actuation of FMμEs by using a rotating NdFeB permanent magnet. A wet etching process was carried out to remove the sacrificial Al layers and release the FMμEs. The magnet was placed ca. 1 cm apart from the FMμEs. The magnetic flux density around the magnetic heads of FMμEs was measured as ~0.05 T (Figure S3). Figures 1g,h illustrate the magnetic torque-induced bending movements of FMμEs by the rotating magnet. Note that only flexible microelectrodes integrated with magnetic microactuators were selectively actuated by magnetic torque (Figure S4). Figure 1i shows a 4-μm-thick and 20-μm-wide FMμE that was helically wound around a 200-μm-diameter optical fiber by using a permanent magnet. These results confirm that remote magnetic actuation can allow facile and controllable positioning of flexible and ultrasmall microelectrodes.

Next, we examined force-driven actuation of FMμEs by magnetic gradients. In order to quantitatively characterize the magnitude of the exerted magnetic forces, the magnetic heads of FMμEs were implemented with stretchable serpentine microsprings (Figure S5). After being released from the Si/SiO$_2$ substrate, an FMμE was exposed to the magnetic field gradient of a permanent magnet at a distance of ca. 2 mm. As shown in Figure 2a,b, the magnetic force dragged the magnetic head of FMμE toward the local maximum of field and stretched the microspring by up to 400 μm. We carried out three-dimensional finite element analysis (FEA) to simulate the stretching process of FMμE by magnetic forces. The initial configuration of FMμE in the FEA was based on the structure of the device shown in Figure 2a. The base plate of FMμE was

fixed in the simulations, and the end-point of FMμE was subjected to a prescribed longitudinal displacement, Δx. Figure 2c shows the stress distribution of FMμE subjected to an elongation of $\Delta x = 400$ μm, which reveals that the stress concentrations are mainly located on the microspring. We then calculated the numerical value of the force, F, exerted on the tip of FMμE at various displacements. As shown in Figure 2d, the force is linearly proportional to the displacement of the microspring, consistent with Hooke's law. The 4-μm-thick and 3.5-μm-wide microspring has a force constant of 2.4 mN/m, and the magnetic force exerted on the tip of FMμE in Figure 2a was thus estimated to be ca. 1 μN. This force value is comparable to contraction forces of single cardiac myocytes.[38,39] These results indicate that remote magnetic actuation of FMμEs may be potentially used for well-controlled mechanical manipulation of biological systems.

Implantable devices that interface with the peripheral nervous system have shown promise for restoring sensory and motor functions in patients who experience neurological injuries or amputations.[5] Over the past decades, intensive research efforts have been focused on reducing the structural and mechanical mismatches between implanted electrodes and peripheral nerve tissues.[40] In particular, flexible peripheral nerve electrodes[3,41,42] have shown improved biocompatibility compared to stiff electrodes. However, the accurate *in vivo* positioning of flexible peripheral nerve electrodes has been challenging. In contrast, the remote magnetic actuation of our FMμEs allows them to interface with the peripheral nerves in a controllable manner. Figure 3a,b shows a 4-μm-thick and 65-μm-wide FMμE array consisting of seven semicircular arch-shaped recording sites and one magnetic microactuator. To the
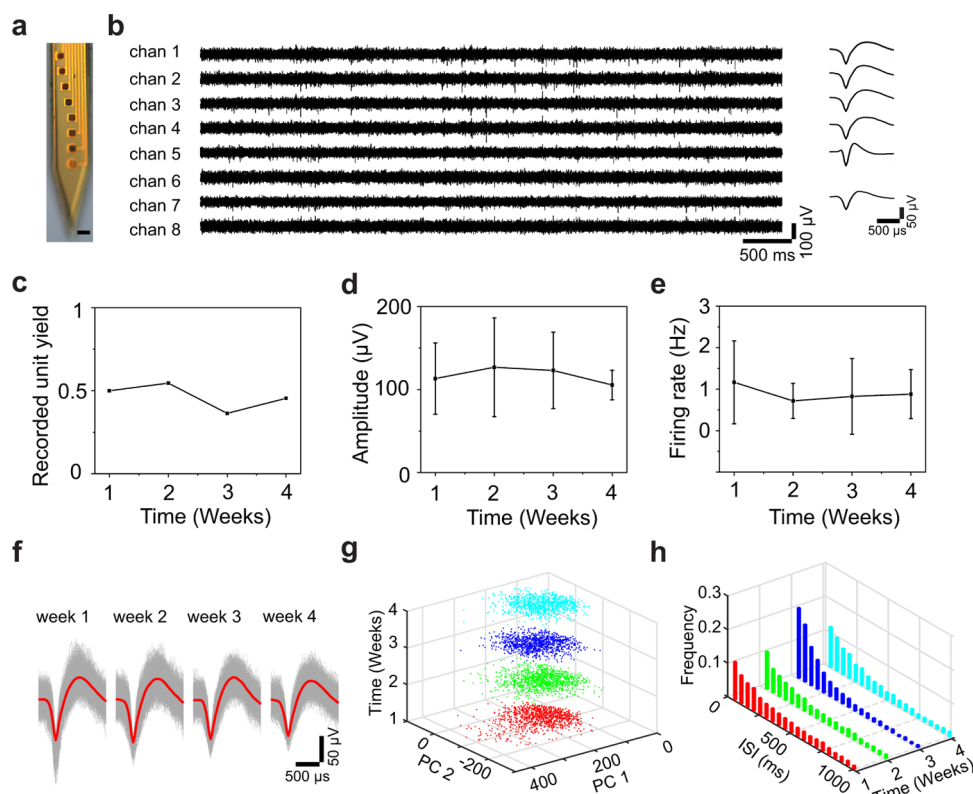
Figure 5. *In vivo* chronic recordings from MO cortex. (a) Optical image of an 8-channel FMμE array. Scale bar, 20 μm. (b) Representative 8-channel AP traces recorded by the FMμE array from MO cortex. (c) Recorded unit yield as a function of time. (d,e) Average spike amplitude and firing rates of all recorded units during the 4-week recording. Error bars represent the SD around the mean. (f) Aligned and averaged spike waveforms of a representative single unit recorded by an FMμE from week-1 to week-4 (>1000 waveforms per average). (g) PCA of all waveforms in (f). (h) Time evolution of ISI histograms for the single unit in (f). Bin size, 50 ms.

best of our knowledge, these are the smallest peripheral nerve microelectrodes ever reported. Before neural recording, platinum was electrodeposited on the recording sites (Figure 3c). The nanoscale roughness of the platinum films effectively increased the active surface areas of the microelectrodes (Figure 3d). As a result, the impedance of the microelectrodes (at 1 kHz) decreased by a factor of ~40 (Figure 3e), which can effectively reduce the thermal noise during neural recordings.[43] The FMμE array was then controllably wound around the distal trunk of a mouse sciatic nerve, with a diameter of only ~400 μm, for desired turns by a permanent magnet placed ca. 3 mm away from the FMμE array (Figures 3f,g and S6). Evoked neural activities were recorded by the FMμE array when monophasic square-wave voltage pulses were applied on the proximal trunk at ~2 mm distance (Figure 3f,g). Former studies have shown that the nerve stimulus threshold is inversely related to the diameter of the motor axons.[44] Thus, large-diameter nerve fibers that are innervated by large motor neurons are the first to be recruited during electrical stimulation.[45] As shown in Figures 3h and S7, the first compound action potential (CAP) from a fast and large-diameter nerve fiber was recorded by the FMμE array at a stimulus voltage of 0.6 V. The CAP propagated from the stimulating electrode to the FMμE array with a conduction latency of 2.5 ± 0.5 ms. When the stimulus voltage was increased to 2.3 V, the CAP from a slow and small-diameter nerve fiber was recorded by the FMμE array, with a conduction latency of 6.7 ± 0.4 ms. Moreover, Figure S8 shows representative multichannel recordings of evoked CAPs in

the mouse sciatic nerve. These results demonstrate that the FMμE array can serve as a facile tool for peripheral nerve interfacing and electrical recordings.

Next, we implanted FMμEs into the secondary motor (M2) cortex of mouse brain for intracortical single-unit recordings. During implantation, a permanent magnet was placed underneath the mouse jaw to adjust the implantation angle of FMμEs. The distance between the magnet and the FMμE was about 12 mm, and the implantation angle of the FMμE was adjusted to be normal to the mouse brain surface. It should be noted that the magnetic gradient of the permanent magnet decreases rapidly with increased distance, and the magnetic forces on the FMμEs were not large enough for tissue penetration.[15] Before implantation, the recording sites of FMμEs were modified with nanorough platinum films to reduce their impedance and thermal noise (Figures 4a,b and S9). The FMμEs were then inserted into the mouse cortex by moving up and down repeatedly until they punctured the tissue (Figures 4c,d and S10). Figure 4e shows a representative action potential (AP) trace recorded by an FMμE. Spike sorting revealed two well-separated neuronal units (L_{ratio} = 0.039 and isolation distance = 47) (Figure 4f−i).[46,47] Moreover, both neurons fired stably during the 3 h recording period, which indicated that they stayed in close proximity to the microelectrode during recording.[2]

We next implanted 8-channel FMμE arrays into the medial orbital (MO) cortex of mice (n = 4) and evaluated their recording stability in a 4-week period. Before implantation, the recording sites of FMμE arrays were modified with nanorough
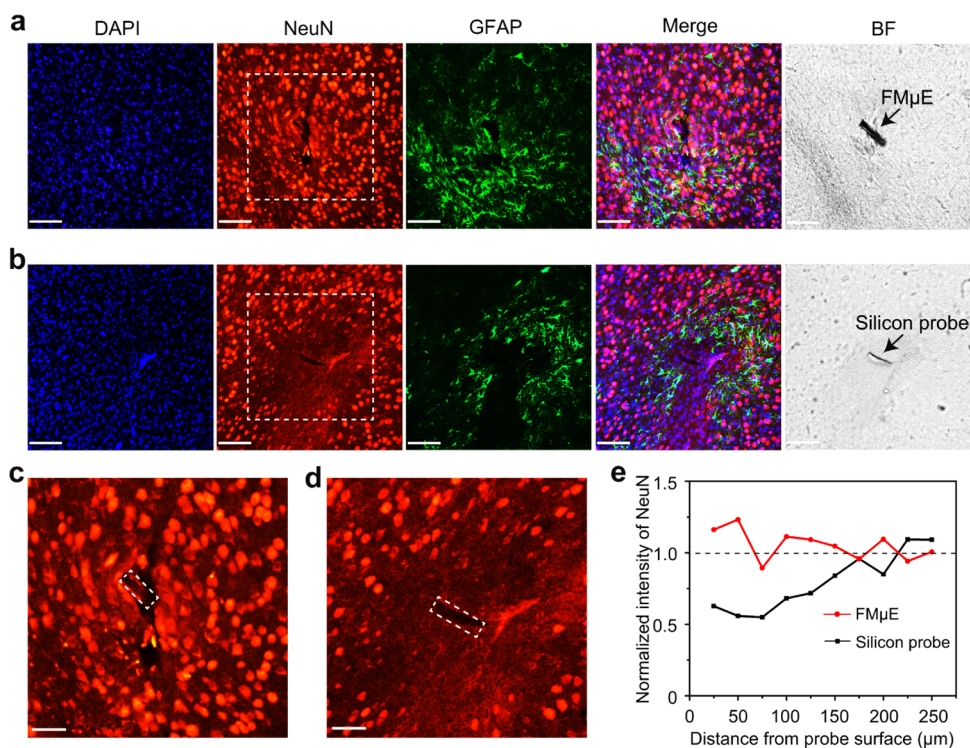
Figure 6. Chronic immune responses to implanted FMμE probe (a) and silicon probe (b). The 100-μm-thick horizontal brain slices were labeled for nuclei (DAPI, blue), neurons (NeuN, red), and astrocytes (GFAP, green), respectively. Scale bar, 100 μm. (c,d) Zoom-in view of the staining images for neurons as marked by the white dashed boxes in (a) and (b), respectively. The edges of the FMμE and silicon probe were highlighted by white dashed boxes. Scale bar, 50 μm. (e) Fluorescence intensity of NeuN normalized against background values was plotted against the distance from surfaces of the FMμE and silicon probe, respectively.

platinum films (Figure 5a). Figure 5b shows representative AP traces recorded by an implanted FMμE array from the MO cortex of a mouse (M01). Single-unit activities were recorded by 6 of the 8 microelectrodes in the FMμE array. Overall, 8–12 units were recorded from 22 FMμEs at a single recording day over the 4-week period, corresponding to a unit yield of 0.4–0.5 (Figure 5c). Moreover, the average spike amplitude and firing rates of the recorded units remained relatively stable (Figure 5d,e). Figure 5f shows the averaged waveforms of a representative unit recorded by an FMμE (M04) from week-1 to week-4. The shape similarity between the averaged waveforms was evaluated by calculating the cross-correlation coefficient.[48] As shown in Table S1, high waveform similarity was observed during the 4-week recording period. Besides, PCA yielded overlapping clusters, and the ISI histograms showed similar distribution patterns from week-1 to week-4 (Figure 5g,h). These results suggest that the recorded single-unit activities might be from the same neuron.[49,50]

Lastly, we evaluated the *in vivo* chronic biocompatibility of FMμEs in mouse brain. For comparison, both FMμEs and conventional silicon probes were implanted into mouse brain. Chronic tissue responses to the implanted probes were evaluated after 5 and 9 weeks postimplantation. Figure 6a,b shows representative immunohistochemical staining results of brain slices implanted with an FMμE and a silicon probe, respectively, at 5 weeks postimplantation. Glial fibrillary acidic protein (GFAP),[51] an intermediate filament of astrocytes, shows increased expression around both the FMμE and the silicon probe at 5 weeks postimplantation. The astrocyte activation extended out ~200 μm around the implantation sites and might be related to the initial wound healing

responses from the insertion injury. Notably, the FMμE and the silicon probe elicited distinctly different neuronal cell responses (Figure 6c–e). As shown in Figure 6d, a clear neuron "kill zone" of 100−200 μm appeared around the silicon probe at 5 weeks postimplantation. This is consistent with former studies showing that the mechanical mismatch and micromotion between stiff silicon probes and neural tissues can induce inflammatory responses and neuronal cell loss around the implantation sites.[9,11] However, minimal neuronal cell loss was observed around the FMμE at 5 weeks postimplantation (Figure 6c). We further evaluated the brain tissue response to an FMμE at 9 weeks postimplantation (Figure S11). No obvious decrease in the density of neuronal cells was observed around the FMμE. Moreover, the density of GFAP-positive astrocytes around the FMμE has reduced to normal levels at 9 weeks postimplantation. These results are consistent with the immunohistochemical results of previously reported flexible probes,[52,53] confirming that FMμEs can form chronically stable interfaces with the central nervous system.

In conclusion, we have fabricated FMμEs that can be remotely actuated by magnetic fields. The FMμEs have been demonstrated for *in vivo* recordings of neural activities from both peripheral nerves and cerebral cortex. Immunohistochemical staining results showed that the chronically implanted FMμEs elicited minimal neuronal cell loss in mouse brain. The FMμEs, therefore, show great promise for the electrical interfacing with biological systems in a minimally invasive manner. The permanent magnets used here, however, are limited in both workspace and degrees of freedom (DoF). Future work will involve the implementation of electro-magnetic actuation systems with a large workspace and high

DoF, as well as high-frequency alternating fields for the controllable navigation of FMμEs amid complex biological systems.[52−58] In addition, MRI systems are routinely used in both basic and clinical neuroscience; thus, future studies are needed to evaluate the biological safety of implanted FMμEs for use in MRI. Nevertheless, the magnetic actuation of ultrasmall FMμEs provides a means to induce micro-Newton forces from a remote distance, which may open up new possibilities for the *in vitro* and *in vivo* mechanical manipulation and electrical probing of neural circuits.

■ ASSOCIATED CONTENT

Ⓢ Supporting Information

The Supporting Information is available free of charge on the ACS Publications website at DOI: 10.1021/acs.nano-lett.9b03232.

Detailed description of experimental methods and additional figures (PDF)

■ AUTHOR INFORMATION

Corresponding Author
*E-mail: fangy@nanoctr.cn.

ORCID Ⓞ
Kun Wu: 0000-0002-1626-396X
Huihui Tian: 0000-0002-9015-4817
Ying Fang: 0000-0003-2965-7287

Author Contributions
∇L.G. and J.W. contributed equally to this work.

Notes
The authors declare no competing financial interest.

■ ACKNOWLEDGMENTS

■ REFERENCES

(1) Donoghue, J. P. *Nat. Neurosci.* **2002**, *5*, 1085−1088.
(2) Buzsáki, G.; Anastassiou, C. A.; Koch, C. *Nat. Rev. Neurosci.* **2012**, *13*, 407−420.
(3) Rodríguez, F. J.; Ceballos, D.; Schüttler, M.; Valero, A.; Valderrama, E.; Stieglitz, T.; Navarro, X. *J. Neurosci. Methods* **2000**, *98*, 105−118.
(4) Miocinovic, S.; Somayajula, S.; Chitnis, S.; Vitek, J. L. *JAMA Neurol.* **2013**, *70*, 163−171.
(5) Navarro, X.; Krueger, T. B.; Lago, N.; Micera, S.; Stieglitz, T.; Dario, P. *J. Peripher. Nerv. Syst.* **2005**, *10*, 229−258.
(6) Rydevik, B. L.; Kwan, M. K.; Myers, R. R.; Brown, R. A.; Triggs, K. J.; Woo, S. L-Y.; Garfin, S. R. *J. Orthop. Res.* **1990**, *8*, 694−701.
(7) Green, M. A.; Bilston, L. E.; Sinkus, R. *NMR Biomed.* **2008**, *21*, 755−764.
(8) Gilletti, A.; Muthuswamy, J. *J. Neural Eng.* **2006**, *3*, 189−195.
(9) Biran, R.; Martin, D. C.; Tresco, P. A. *Exp. Neurol.* **2005**, *195*, 115−126.
(10) Kozai, T. D. Y.; Jaquins-Gerstl, A. S.; Vazquez, A. L.; Michael, A. C.; Cui, X. T. *ACS Chem. Neurosci.* **2015**, *6*, 48−67.
(11) Polikov, V. S.; Tresco, P. A.; Reichert, W. M. *J. Neurosci. Methods* **2005**, *148*, 1−18.
(12) Kim, T.-i.; McCall, J. G.; Jung, Y. H.; Huang, X.; Siuda, E. R.; Li, Y.; Song, J.; Song, Y. M.; Pao, H. A.; Kim, R.-H.; Lu, C.; Lee, S. D.; Song, I.-S.; Shin, G.; Al-Hasani, R.; Kim, S.; Tan, M. P.; Huang, Y.; Omenetto, F. G.; Rogers, J. A.; Bruchas, M. R. *Science* **2013**, *340*, 211−216.
(13) Khodagholy, D.; Gelinas, J. N.; Thesen, T.; Doyle, W.; Devinsky, O.; Malliaras, G. G.; Buzsáki, G. *Nat. Neurosci.* **2015**, *18*, 310−315.
(14) Liu, J.; Fu, T.-M.; Cheng, Z.; Hong, G.; Zhou, T.; Jin, L.; Duvvuri, M.; Jiang, Z.; Kruskal, P.; Xie, C.; Suo, Z.; Fang, Y.; Lieber, C. M. *Nat. Nanotechnol.* **2015**, *10*, 629−636.
(15) Luan, L.; Wei, X.; Zhao, Z.; Siegel, J. J.; Potnis, O.; Tuppen, C. A.; Lin, S.; Kazmi, S.; Fowler, R. A.; Holloway, S.; Dunn, A. K.; Chitwood, R. A.; Xie, C. *Sci. Adv.* **2017**, *3*, No. e1601966.
(16) Kozai, T. D. Y.; Gugel, Z.; Li, X.; Gilgunn, P. J.; Khilwani, R.; Ozdoganlar, O. B.; Fedder, G. K.; Weber, D. J.; Cui, X. T. *Biomaterials* **2014**, *35*, 9255−9268.
(17) Xiang, Z.; Yen, S.-C.; Xue, N.; Sun, T.; Tsang, W. M.; Zhang, S.; Liao, L.-D.; Thakor, N. V.; Lee, C. *J. Micromech. Microeng.* **2014**, *24*, No. 065015.
(18) Vitale, F.; Vercosa, D. G.; Rodriguez, A. V.; Pamulapati, S. S.; Seibt, F.; Lewis, E.; Yan, J. S.; Badhiwala, K.; Adnan, M.; Royer-Carfagni, G.; Beierlein, M.; Kemere, C.; Pasquali, M.; Robinson, J. T. *Nano Lett.* **2018**, *18*, 326−335.
(19) Nelson, B. J.; Kaliakatsos, I. K.; Abbott, J. J. *Annu. Rev. Biomed. Eng.* **2010**, *12*, 55−85.
(20) Dobson, J. *Nat. Nanotechnol.* **2008**, *3*, 139−143.
(21) Peyer, K. E.; Zhang, L.; Nelson, B. J. *Nanoscale* **2013**, *5*, 1259−1272.
(22) Eichenfield, M.; Michael, C. P.; Perahia, R.; Painter, O. *Nat. Photonics* **2007**, *1*, 416−422.
(23) Luo, X.; Mather, P. T. *Soft Matter* **2010**, *6*, 2146−2149.
(24) Moulton, T.; Ananthasuresh, G. K. *Sens. Actuators, A* **2001**, *90*, 38−48.
(25) Choi, H.; Choi, J.; Jang, G.; Park, J.-o.; Park, S. *Smart Mater. Struct.* **2009**, *18*, No. 055007.
(26) Sánchez, S.; Pumera, M. *Chem. - Asian J.* **2009**, *4*, 1402−1410.
(27) Xu, T.; Yu, J.; Yan, X.; Choi, H.; Zhang, L. *Micromachines* **2015**, *6*, 1346−1364.
(28) Polyak, B.; Fishbein, I.; Chorny, M.; Alferiev, I.; Williams, D.; Yellen, B.; Friedman, G.; Levy, R. J. *Proc. Natl. Acad. Sci. U. S. A.* **2008**, *105*, 698−703.
(29) Lübbe, A. S.; Alexiou, C.; Bergemann, C. *J. Surg. Res.* **2001**, *95*, 200−206.
(30) Wilson, B.; Samanta, M. K.; Santhi, K.; Sampath Kumar, K. P.; Ramasamy, M.; Suresh, B. *J. Neurosci. Methods* **2009**, *177*, 427−433.
(31) Vach, P. J.; Brun, N.; Bennet, M.; Bertinetti, L.; Widdrat, M.; Baumgartner, J.; Klumpp, S.; Fratzl, P.; Faivre, D. *Nano Lett.* **2013**, *13*, 5373−5378.
(32) Peyer, K. E.; Tottori, S.; Qiu, F.; Zhang, L.; Nelson, B. J. *Chem. - Eur. J.* **2013**, *19*, 28−38.
(33) Mathieu, J.-B.; Martel, S. *Biomed. Microdevices* **2007**, *9*, 801−808.
(34) Koohkan, R.; Sharafi, S.; Shokrollahi, H.; Janghorban, K. *J. Magn. Magn. Mater.* **2008**, *320*, 1089−1094.
(35) Cao, Y.; Wei, G. Y.; Ge, H. L.; Meng, X. F. *Surf. Eng.* **2014**, *30*, 97−101.
(36) Zhou, L.; Wen, M.; Wu, Q.; Wu, D. *Dalton Trans.* **2014**, *43*, 7924−7929.
(37) Su, X.; Qiang, C. *Bull. Mater. Sci.* **2012**, *35*, 183−189.
(38) Kajzar, A.; Cesa, C. M.; Kirchgeßner, N.; Hoffmann, B.; Merkel, R. *Biophys. J.* **2008**, *94*, 1854−1866.
(39) Yasuda, S.-I.; Sugiura, S.; Kobayakawa, N.; Fujita, H.; Yamashita, H.; Katoh, K.; Saeki, Y.; Kaneko, H.; Suda, Y.; Nagai, R.; Sugi, H. *Am. J. Physiol. Heart Circ. Physiol.* **2001**, *281*, H1442−H1446.

(40) Christensen, M. B.; Pearce, S. M.; Ledbetter, N. M.; Warren, D. J.; Clark, G. A.; Tresco, P. A. *Acta Biomater.* **2014**, *10*, 4650−4660.

(41) Wurth, S.; Capogrosso, M.; Raspopovic, S.; Gandar, J.; Federici, G.; Kinany, N.; Cutrone, A.; Piersigilli, A.; Pavlova, N.; Guiet, R.; Taverni, G.; Rigosa, J.; Shkorbatova, P.; Navarro, X.; Barraud, Q.; Courtine, G.; Micera, S. *Biomaterials* **2017**, *122*, 114−129.

(42) Xue, N.; Sun, T.; Tsang, W. M.; Delgado-Martinez, I.; Lee, S.-H.; Sheshadri, S.; Xiang, Z.; Merugu, S.; Gu, Y.; Yen, S.-C.; Thakor, N. V. *Sens. Actuators, B* **2015**, *210*, 640−648.

(43) Rios, G.; Lubenov, E. V.; Chi, D.; Roukes, M. L.; Siapas, A. G. *Nano Lett.* **2016**, *16*, 6857−6862.

(44) Zimmermann, M. *Science* **1968**, *160*, 896−898.

(45) Llewellyn, M. E.; Thompson, K. R.; Deisseroth, K.; Delp, S. L. *Nat. Med.* **2010**, *16*, 1161−1165.

(46) Lewicki, M. S. *Network: Comput. Neural Syst.* **1998**, *9*, R53−R78.

(47) Schmitzer-Torbert, N.; Jackson, J.; Henze, D.; Harris, K.; Redish, A. D. *Neuroscience* **2005**, *131*, 1−11.

(48) Jackson, A.; Fetz, E. E. *J. Neurophysiol.* **2007**, *98*, 3109−3118.

(49) Fu, T. M.; Hong, G.; Zhou, T.; Schuhmann, T. G.; Viveros, R. D.; Lieber, C. M. *Nat. Methods* **2016**, *13*, 875−882.

(50) Hong, G.; Lieber, C. M. *Nat. Rev. Neurosci.* **2019**, *20*, 330−345.

(51) Bignami, A.; Eng, L. F.; Dahl, D.; Uyeda, C. T. *Brain Res.* **1972**, *43*, 429−435.

(52) Xie, C.; Liu, J.; Fu, T.-M.; Dai, X.; Zhou, W.; Lieber, C. M. *Nat. Mater.* **2015**, *14*, 1286−1292.

(53) Zhou, T.; Hong, G.; Fu, T.-M.; Yang, X.; Schuhmann, T. G.; Viveros, R. D.; Lieber, C. M. *Proc. Natl. Acad. Sci. U. S. A.* **2017**, *114*, 5894−5899.

(54) Vollmers, K.; Frutiger, D. R.; Kratochvil, B. E.; Nelson, B. J. *Appl. Phys. Lett.* **2008**, *92*, 144103.

(55) Kummer, M. P.; Abbott, J. J.; Kratochvil, B. E.; Borer, R.; Sengul, A.; Nelson, B. J. *IEEE T. Robot.* **2010**, *26*, 1006−1017.

(56) Dryg, I. D.; Ward, M. P.; Qing, K. Y.; Mei, H.; Schaffer, J. E.; Irazoqui, P. P. *IEEE T. Neur. Sys. Reh.* **2015**, *23*, 562−571.

(57) Diller, E.; Giltinan, J.; Lum, G. Z.; Ye, Z.; Sitti, M. *Int. J. Robot. Res.* **2016**, *35*, 114−128.

(58) Chen, X.-Z.; Hoop, M.; Mushtaq, F.; Siringil, E.; Hu, C.; Nelson, B. J.; Pané, S. *Appl. Mater. Today* **2017**, *9*, 37−48.